RSC Advances

REVIEW

View Article Online
View Journal | View Issue

Cite this: *RSC Adv.*, 2025, **15**, 9555

Review of MXene synthesis and applications in electromagnetic shielding

Yao Gan and Yuzhu Xiong *

With the ongoing advancements in wireless communication and electronic technology, the issue of electromagnetic radiation (EMR) pollution has become increasingly significant. Consequently, developing materials to mitigate EMR pollution is essential. The utility of 2D MXene ($Ti_3C_2T_x$) for electromagnetic interference (EMI) shielding was initially reported in 2016. Since then, MXenes have garnered substantial interest from the scientific community owing to their excellent metallic conductivity, low density, expansive specific surface area, and tunable interlayer spacing. In recent years, MXenes have demonstrated considerable promise in EMI shielding applications. This paper aims to examine the structural and chemical properties of MXenes, the methodologies for their synthesis, and summarize the advancements in MXene-based EMI shielding composites, highlighting their performance benefits. Additionally, this review will discuss the prospective developments in MXene-based materials for EMI shielding.

Received 12th November 2024
Accepted 6th March 2025

DOI: 10.1039/d4ra08030k

rsc.li/rsc-advances

1 Introduction

Electromagnetic waves serve as a critical medium for information transmission, possessing the unique ability to propagate through vacuous space, thereby facilitating long-distance communication.[1–3] With the advancement of technology and the integration of 5G communications into daily life, our reliance on electromagnetic applications, such as wireless communication, television, computers, global positioning systems, and radar detectors, continues to grow.[3–7] However, excessive exposure to electromagnetic waves can lead to significant electromagnetic radiation pollution, posing unseen and silent threats.[8] In the era of electronic information, electromagnetic radiation can disrupt the function of electronic devices in military, industrial, and residential settings, potentially posing severe risks to human health and the biosphere.[1,5,7,9–14] Consequently, developing effective EMI shielding materials is crucial to safeguard both the functionality of electronic devices and public health.

EMI shielding is a critical strategy for mitigating EMR pollution. This process involves the attenuation or complete shielding of electromagnetic waves by specific materials, thereby ensuring the smooth operation of sensitive equipment and protecting humans from EMR exposure.[15–17] Although traditional metal shielding materials, characterized by high conductivity, are effective in reflecting electromagnetic waves, this attribute also leads to secondary reflections of these waves, contributing to contamination. Moreover, these materials often suffer from high density, corrosion susceptibility, and complex

Department of Materials and Metallurgy, Guizhou University, Guiyang 550025, China. E-mail: xyzhu789@126.com

Yao Gan

Yao Gan is studying in the Department of Materials and Chemical Engineering, College of Materials and Metallurgy, Guizhou University. Her main research area is the structure and properties of polymer matrix composites. Email address: gyao0311@163.com.

Yuzhu Xiong

Yuzhu Xiong, a professor at Guizhou University, focuses on research into the structure and properties of polymer matrix composites. Email address: xyzhu789@126.com.

manufacturing processes, which restrict their broader application.[18,19] Consequently, researchers have been developing alternative shielding materials, such as graphene, carbon nanotubes, and MXene, which offer corrosion resistance, reduced weight, and enhanced performance.

Since the introduction of graphene in 2004, two-dimensional materials have garnered significant interest, as illustrated in Fig. 1. The family of transition metal carbides, nitrides, and carbonitrides, collectively known as MXenes, has particularly drawn global research attention since its first discovery in 2011. These materials are prized for their metallic conductivity, optical properties, and surfaces enriched with functional groups and hydrophilic sites.[20–27] A landmark achievement was realized in 2016 when Yury Gogotsi's team advanced from theoretical concepts to practical applications in EMI shielding using 2D materials. They developed a highly flexible MXene film with a thickness of 45 μm, which demonstrated the ability to block 99.99999999999994% of incident radiation, achieving a shielding effectiveness of 92 dB. This performance is on par with that of traditional metal shields.[28]

MXene is composed of transition metal elements, along with carbon and nitrogen, and is characterized by high electrical and thermal conductivity, as well as a multitude of surface functional groups that enhance its surface reactivity.[29] The precursor to MXene, known as the MAX phase, belongs to the hexagonal crystalline system. In this system, 'M' denotes the transition metal, 'A' represents an element from either the III or IV main group, and 'X' indicates an element of carbon or nitrogen. The atomic layers of "M" and "X" are interleaved, and both are bonded by a mixture of ionic and covalent bonds. In contrast, the 'A' atomic layer is interspersed through metallic bonding. This configuration hinders the mechanical delamination of MXene due to the strong M–X bond energy compared to the M–A bond, which exhibits greater chemical activity.[30] Consequently, selective etching can preferentially disrupt the active M–A bonds to produce 2D MXene materials.[31–33] Notably, MXene's excellent electrical conductivity facilitates the improvement of material impedance mismatch, enhancing the reflection of electromagnetic waves or boosting electromagnetic loss capabilities for effective absorption. This leads to outstanding electromagnetic shielding performance.[34,35]

This paper provides a comprehensive review of the structure, properties, and preparation methods of MXene, as well as the applications of MXene-based composites in the field of electromagnetic shielding. It also summarizes the challenges associated with the current preparation methods and yields of MXene. Furthermore, the paper explores future prospects for the application of MXene in electromagnetic shielding.

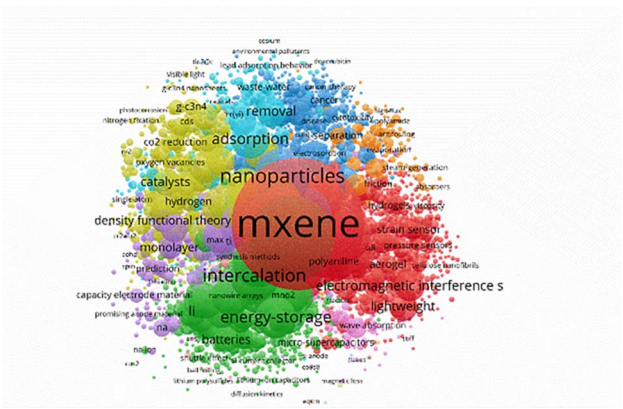

Fig. 1 Network view of the structural distribution of MXene research hotspots 2012–2023.

2 Studies on the structure, properties and preparation of MXene

2.1 Structure of MXene

MXene is an innovative two-dimensional material characterized by a unique layered structure reminiscent of graphene's hexagonal honeycomb pattern. Each layer is composed of hexagonal transition metal carbides, nitrides, or carbonitrides. The layers of MXene are interconnected and self-stacked through van der Waals forces, electrostatic interactions, and hydrogen bonds, permitting some degree of relative sliding.[36] However, the self-stacking of MXene layers, predominantly driven by van der Waals forces, often leads to reduced electronic pathways, thereby diminishing the material's electrochemical performance.[37–40] The chemical composition of MXene is typically denoted by the formula $M_{n+1}X_nT_x$, where 'M' represents transition metal elements, 'X' denotes mainly elements carbon and nitrogen, 'n' indicates the number of elements in the interlayer voids, and 'T' refers to surface functional groups, including –OH, –F, –O, or –Cl[41–43] (Fig. 2).

Recent advancements in MXene research have led to its evolution from the initial accordion-like structure to contemporary forms such as nanoribbons, hollow spheres, and porous structures. Zeng *et al.* synthesized lamellar MXene, networked MXene nanoribbons, and porous lamellar MXene by employing strategies involving hydrofluoric acid etching, KOH shear, and high-temperature molten salts.[44] These modifications enhance surface states and microstructures, significantly boosting the absorption of electromagnetic waves. Notably, the networked MXene nanoribbons exhibited reflection loss values as high as −63.01 dB. Moreover, the network structure of MXene nanosheets with low defects and large dimensions is more effective in increasing the conductivity of the material, thus further improving its electromagnetic shielding properties.[45] The surface functional groups (*e.g.*, –OH, –F) of the conductive MXene induce local dipoles under electric and magnetic fields, leading to polarization losses of electromagnetic waves. When electromagnetic waves transit through multiple layers of MXene nanosheets, they undergo multiple reflections and dissipations, similar to the described energy loss mechanisms, ultimately resulting in substantial electromagnetic wave attenuation,[46,47] as depicted in Fig. 3.

2.2 Properties of MXene

The structural features of MXene fundamentally determine its properties, which in turn facilitate a broad spectrum of applications across various potential fields.

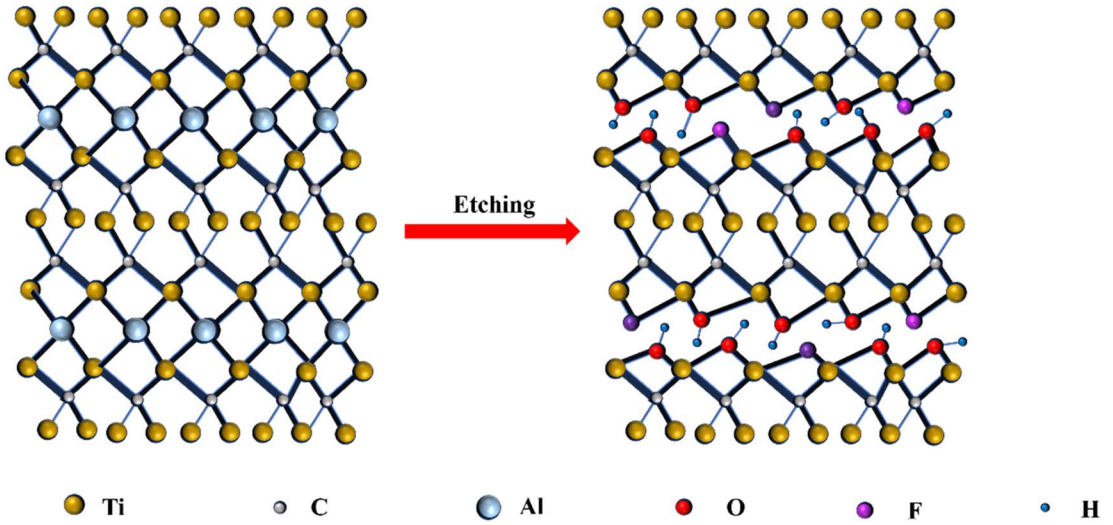

Fig. 2 Schematic representation of the MXene structure derived from Ti_3AlC_2 MAX phase.

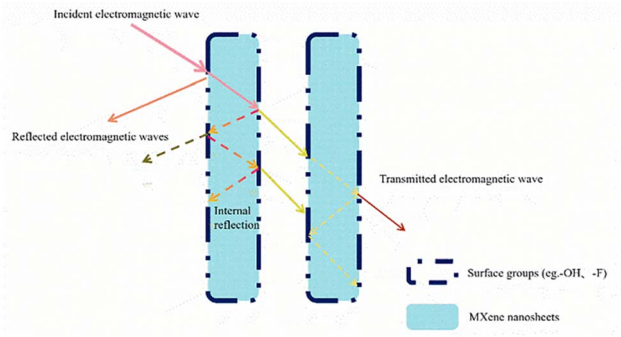

Fig. 3 Schematic diagram of EMI shielding mechanism of MXene nanosheets.

2.2.1 Electrical conductivity. The electrical conductivity of MXene is a pivotal property, directly influencing its application in electrochemical devices, lithium-ion batteries, and capacitors. Notably, MXene's superior conductivity provides significant advantages in the field of electromagnetic shielding.[48] Variations in material types and preparation conditions yield substantial differences in product size and surface functional groups, which in turn impact their electrochemical structures.

Kathleen Maleski *et al.* produced $Ti_3C_2T_x$ nanosheets of varying sizes using acoustic wave treatment and density gradient centrifugation.[49] They discovered that films made from larger MXene nanosheets exhibited a peak conductivity of approximately 5000 S cm^{-1}. In contrast, films from smaller MXene sheets demonstrated a significantly reduced conductivity of only 1000 S cm^{-1}. This conductivity is lower than that of carbon-based MXene, which was initially synthesized using the *in situ* generation of hydrofluoric acid method.[50] Utilizing the density-functional tight-binding (DFTB) method, Khanal *et al.* explored the influence of MXene surface functional groups and their ratios on electrical conductivity.[51] Notably, unmodified MXene surfaces exhibited higher electrical conductivity compared to those modified by –OH, which in turn showed higher conductivity than MXene surfaces altered by –O. Furthermore, conductivity varied depending on the ratios of –O to –OH. Eom *et al.* annealed $Ti_3C_2T_x$-MXene monolayer nanosheets under argon and ammonia atmospheres, revealing that nitridation in ammonia not only preserved the electron-rich structure of Ti_3C_2 but also doubled the conductivity compared to the argon-treated MXene films.[52] Mathis *et al.* synthesized MAX powders with a high aluminum content and prepared monolayer MXene sheets with minimal defects and large dimensions (maximum size > 25 μm) by etching, washing, and centrifugation of the precursor.[53] These sheets achieved an electrical conductivity as high as 20 000 S cm^{-1}, attributable to their large layer sizes and fewer defects, which enhanced in-sheet electron transfer capability and chemical stability. Such high conductivity positions MXene favorably for development in electromagnetic shielding applications.

2.2.2 Magnetic properties. MXene exhibits potential magnetic properties as most non-terminated MXenes are inherently magnetic; however, the introduction of termination groups can significantly alter these properties.[32] Building on this, researchers have successfully imparted magnetic properties to MXene by incorporating magnetic ions or nanoparticles. It is important to note that the magnetic characteristics of MXene-based materials are influenced by several factors, including the surface properties of MXene, the type and quantity of transition metal ions, and the size and morphology of the magnetic nanoparticles.

Zhang *et al.* enhanced the magnetic properties of MXene by annealing a monolayer of $Ti_3C_2T_x$-MXene to induce the formation of amorphous carbon on the sample surface.[54] Liu *et al.* coated Ti_3C_2-MXene with superparamagnetic iron oxide nanoparticles, successfully creating magnetic MXene composites for highly efficient cancer therapy diagnostics.[55] This material is not only beneficial for enhancing magnetic resonance imaging of tumors but also effective in the photothermal eradication of

cancer cells and tumor tissue ablation. Building on the platform of 3D MXene induced by ethylenediamine, Zhang *et al.* synthesized a magnetic aerogel with a porous structure by the *in situ* co-precipitation of iron tetraoxide on 3D MXene.[56] This unique structure demonstrated the capability to remove up to 2385 mg g^{-1} of silver from water through adsorption.

2.2.3 Other properties. It is well known that carbon and nitrogen, which are fundamental elements in biological structures, are also primary constituents of MXenes, thereby conferring biocompatibility on these materials. Additionally, MXene possesses antimicrobial therapeutic properties and has been utilized in various antimicrobial materials and drug carriers to treat bacterial infections.[57–59] This efficacy stems from MXene's ability to adsorb onto bacterial membranes, inducing localized phase transitions that lead to leakage of intracellular molecules and subsequent cell inactivation through lysis.[60] The densely packed laminar structure and very fine lattice configuration of MXene impart high thermal conductivity, positioning it as a promising material for thermal management applications. Wei *et al.* have enhanced the thermal conductivity of epoxy composites by integrating a framework of hollow MXene spheres, thereby achieving superior thermal conductivity.[61]

2.3 Preparation method of MXene

MXene, a novel two-dimensional material, has experienced rapid development across various fields due to its advantageous properties, including high electrical conductivity, high elastic modulus, large specific surface area, and adjustable hydrophilic surface. It shows particularly strong potential in microwave absorption and electromagnetic shielding.[62,63] In the crystal structure of the MAX phase, the M–X bonding energy, which can be covalent or ionic, is significantly higher than the M–A bonding energy, which is metallic. Under certain conditions, the A layer in the MAX phase can be exfoliated to produce MXene.[64] The preparation method of MXene influences its elemental composition, morphology, and surface functional groups, subsequently affecting its properties. Therefore, MXenes are selected based on the specific requirements of different practical applications. Currently, several established methods are employed for MXene preparation, including: hydrofluoric acid (HF) etching, *in situ* HF generation etching, fluoride molten salt etching, ultrasound-assisted etching, alkali solution-assisted etching, electrochemical anodic etching, Lewis acidic molten salt etching, and gas-phase dry etching.

2.3.1 Hydrofluoric acid etching. In 2011, Naguib *et al.* immersed milled Ti_3AlC_2 powder in hydrofluoric acid solution at room temperature.[21] After several washes with deionized water, they successfully exfoliated the Al atomic layer from the precursor and, for the first time, obtained a two-dimensional nanomaterial, Ti_3C_2, with an accordion-like structure. The structure and properties of this selectively etched two-dimensional carbide were found to be similar to those of graphene. The etched MXene surface carries a significant number of functional groups, including –OH, –F, and –O, which endow it with unique chemical properties. This selective etching of the MAX phase successfully transformed the three-dimensional crystal structure into a two-dimensional one, providing a novel approach for synthesizing two-dimensional materials and laying the groundwork for expanding the MXene family. Further developments were made by Huang *et al.*, who prepared the adsorbent Ti_3C_2-MXene for the adsorption of sodium bis(-chlorophenolate) through hydrofluoric acid etching of Ti_3AlC_2, followed by solvent heat treatment to form TiO_2 and Ti_2C.[65] This process enhanced the performance of MXene for adsorption under various pH conditions, demonstrating significant potential for environmental protection applications.

2.3.2 *In situ* generation of hydrofluoric acid etching. Hydrofluoric acid poses significant risks to both human health and the environment during its use in material preparation. Consequently, the development of milder, safer, and more reliable methods is crucial for the large-scale production and application of MXene. In 2014, Ghidiu *et al.* first replaced hydrofluoric acid with a mixture of hydrochloric acid and lithium fluoride to etch Ti_3AlC_2, successfully producing a black 'clay' ($Ti_3C_2T_x$-MXene) that exhibited high yield and high electrical conductivity (1500 S cm^{-1}).[50] This method yields a MXene surface with enhanced hydrophilicity and plasticity, due to the presence of –Cl, in addition to –OH, –F, and –O functional groups, compared to surfaces prepared by direct etching with hydrofluoric acid. Notably, lithium ions served as an intercalating agent, collaborating with water molecules to expand the layer spacing of $Ti_3C_2T_x$. Diverging from previous techniques using water as a medium, Soundiraraju *et al.* immersed ball-milled Ti_2AlN powder in a mixed solution of potassium fluoride and hydrochloric acid, reacting it at 40 °C for 3 hours to produce a less-layered nitrogen-containing 2D material, Ti_2N-MXene.[66]

To further examine the characteristics of the *in situ* generation of hydrofluoric acid (HFA) method, Zhang *et al.* assessed the impact of time and concentration of hydrofluoric acid on etching efficiency.[67] They compared the efficiency and electrochemical properties of $Ti_3C_2T_x$-MXene prepared by both the direct use of hydrofluoric acid and the *in situ* generation of HFA. Although both methods effectively removed the Al layer, significant differences were observed in the products: (1) MXene etched directly with hydrofluoric acid displayed an accordion-like morphology under microscopic examination, while products from the *in situ* generation method exhibited a pleated structure; (2) MXene prepared *via* the *in situ* generation of HFA at 10 mV S^{-1} demonstrated a higher specific capacitance and superior electrochemical performance compared to those prepared by the direct hydrofluoric acid method. This enhanced performance is primarily attributed to the use of an intercalation agent in the *in situ* generation process, which contains lithium ions that expand the lattice space of the sample, thereby improving the ion transport environment.

2.3.3 Fluorinated molten salt etching. Although most of the etching systems used for the preparation of MXene are HF-containing solutions, it takes a lot of time to completely etch the 'A' layer in this system, which can be found in most of the studies of this system: the etching time of this system is at least 24 h. Based on the problems of etching in traditional HF-

containing solutions, Wang *et al.* successfully prepared MXene in only 5 min by using molten salt pairs at a lower temperature of 130 °C.[68] In addition, they applied this low-temperature molten salt method to other MAX-like phases. Among them, vanadium-based MXene not only exhibits excellent cycling stability when used as an electrode material, but also has the ability to facilitate rapid charge transport. This is due to the fact that the high-speed flowing molten salt acts as an 'intercalating agent', which enlarges the spacing between the MXene layers and facilitates the transport of electrons. Arole *et al.* prepared water-dispersible Nb_2CT_x nanosheets by etching with molten salt SnF_2 and washing with potassium hydroxide, noting a 23% increase in oxide presence on the surface of the nanosheets after 300 hours of storage, indicating poor oxidative stability.[69]

2.3.4 Ultrasound-assisted etching. In some liquid-phase etching methods, ultrasound-assisted etching is an essential operation, because ultrasound is beneficial for us to obtain monolayer or few-layer MXene, but improper operation tends to fragment the MXene, and the ultrasound process generates heat to oxidize the MXene nanosheets. In contrast to conventional stir etching methods, Yao *et al.* used a mixture of NaF/HF and HCl as etchant and utilized high-intensity ultrasonic exfoliation (HIUE) to prepare MXene with tunable bandgap, high conductivity, and large specific surface area for gas sensing applications.[70] Most importantly, the HIUE method not only reduced the preparation time significantly, from 24/48 hours to 3 hours, but also increased the yield of MXene, demonstrating its efficiency over other methods as illustrated in Fig. 1(c and d).

2.3.5 Alkali solution assisted etching. Although fluoride ions are crucial in the preparation of MXene, the presence of a large number of –F functional groups on its surface can significantly impair the electrochemical properties and stability of the product, while the use of fluorinating agents poses additional environmental hazards.[71–74] From a kinetic perspective, the etching of titanium aluminum carbide by alkaline solutions is impeded by the surface oxides. However, the refinement of bauxite in the Bayer process has demonstrated that elevated temperatures and increased alkaline solution concentrations facilitate the dissolution of aluminum oxides or aluminum hydroxides. Utilizing the conventional Bayer method of bauxite extraction, Li *et al.* synthesized high-purity multilayered $Ti_3C_2T_x$-MXene with oxygen-containing terminals employing a sodium hydroxide-based solution-assisted hydrothermal method at 270 °C.[75]

The majority of studies concerning the stability of MXene have indicated that the introduction of surface termination groups is influenced by the etching method utilized, which subsequently impacts the stability of MXene.[76] Thus, Xue *et al.* employed a tetramethylammonium hydroxide (TMAOH) solution for the etching of MAX, leading to the formation of oxygen-terminated O-MXene.[73] In contrast to MXene with fluorine terminations, which were produced through the *in situ* generation of hydrofluoric acid (HF), O-MXene exhibited superior antioxidant properties and demonstrated a reduced degradation rate in aqueous dispersions. This enhanced stability may be attributed to the greater electron-absorbing capacity of oxygen compared to fluorine, which renders titanium more favorable towards oxygen, resulting in a higher oxidation state of titanium. Additionally, it is plausible that the bonding energy of the titanium–oxygen bond surpasses that of the titanium–fluorine bond.[73,77]

2.3.6 Electrochemical anodic etching (EAE). In a distinct approach, Sheng *et al.* transformed Mo_2TiAlC_2 into three-dimensional structured MXene in a short period by combining anodic electrochemical *in situ* aluminum etching with cathodic electrophoretic deposition.[78] Yang *et al.* employed a binary aqueous solution system for etching, achieving a material with high surface area and bulk capacitance.[79] The

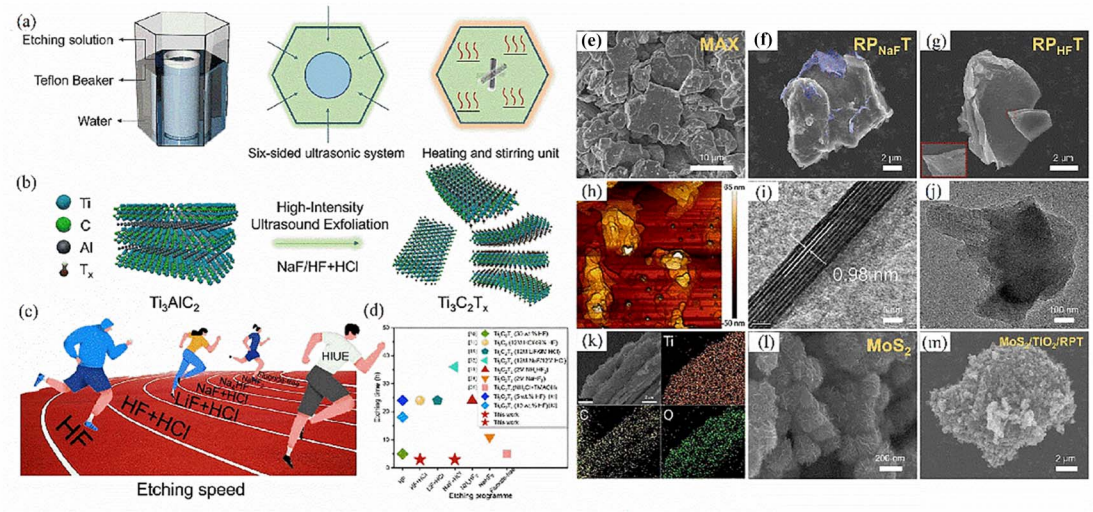

Fig. 4 (a) Schematic diagram of conditions and equipment for HIUE method preparation, (b) schematic diagram of etchant mechanism for HIUE method, (c) etching speed of HIUE method is ahead of other etching methods, (d) comparison of time between HIUE method and other etching methods, (e–g) SEM images of the rapid preparation of MXene by HIUE using NaF and HF as etchant, (h–j) AFM, HRTEM and TEM images of the products of this rapid preparation method (RPT), (k) SEM-EDS images of RPT with respect to the elements Ti, C and O, (l and m) MoS_2 and MoS_2/TiO_2/RPT SEM images. Reproduced from ref. 70 with permission from [Elsevier], copyright [2024].

extraction of MXene flakes was efficiently accomplished through anodic etching of Ti_3AlC_2, dissolution of Al, and *in situ* intercalation of ammonium hydroxide.

2.3.7 Lewis acid molten salt etching. The distinctive chemical properties of the Lewis acid molten salt as an etchant facilitate precise regulation of the surface functional groups and structural features of MXene during the reaction process, thereby enabling customized optimization of MXene properties. Furthermore, the Lewis acid molten salt etching technique demonstrates considerable versatility and can be applied to the etching of various MAX-phase precursors, significantly expanding the diversity and structural variety of MXenes. Of paramount importance, this method not only circumvents the safety concerns and environmental pollution issues associated with the conventional HF etching method but also provides a safer, more controllable, and environmentally sustainable approach for the synthesis of MXene. Li *et al.* were the first to obtain pure Cl-terminated MXene materials using zinc ions in the Lewis acidic molten salt $ZnCl_2$ to displace Al elements in the MAX phase.[80] Additionally, the experimental results further confirmed that for the MAX phase with high M–A bonding energy, conventional HF etching requires a longer time and higher concentration. Consequently, this method not only provides an environmentally sustainable synthetic pathway for the preparation of MXene but also presents a novel approach for efficient synthesis.

2.3.8 Gas-phase dry assisted etching. In most of the previous studies on MXene preparation, the precursors were etched in the liquid phase. Contrasting these approaches, Zhu *et al.* introduced a mild, green, and scalable method for preparing fluorine-free MXene, termed 'gas-phase selective dry etching'.[81] By altering the etching gas to a fluorine-free option and adjusting the ratio of element A in the MAX phase, they successfully prepared $Ti_3C_2Cl_2$-MXene with exceptional capacitance performance and cycling stability, as depicted in Fig. 5(a and b). The etching of the corresponding 'A' layer using a halogen gas with strong oxidizing power not only precisely controls the elements of the MXene end-groups but also produces a by-product, hydrogen halide gas, which can be directly collected for use in other areas. In addition, the end product of this method is a powder that does not require sonication, drying, *etc.*, which effectively improves the work efficiency and provides a new idea for the preparation of MXene.

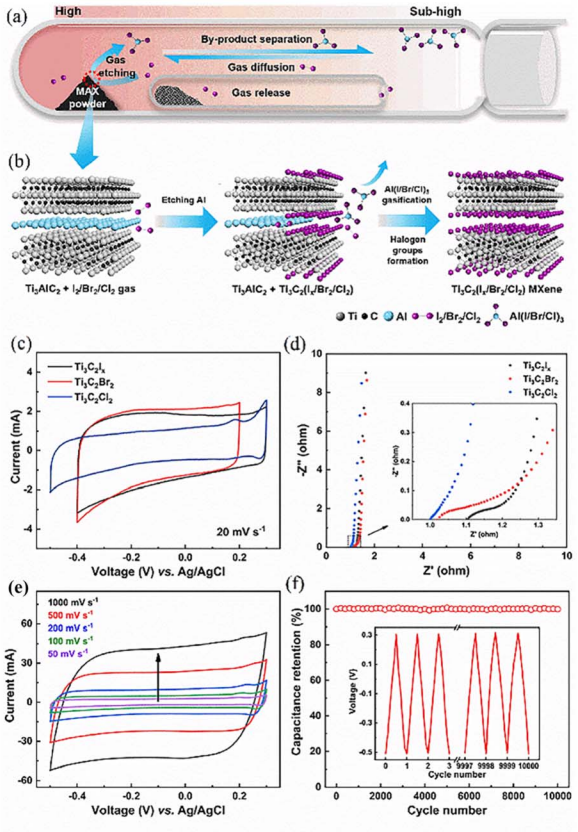

Fig. 5 (a and b) Mechanism of gas-phase selective dry etching, (c) CV curves of $Ti_3C_2I_x$, $Ti_3C_2Br_2$, and $Ti_3C_2Cl_2$ at a scan rate of 20 mV s^{-1}, (d) EIS curves of $Ti_3C_2I_x$, $Ti_3C_2Br_2$, and $Ti_3C_2Cl_2$; (e) CV curves of $Ti_3C_2I_x$, $Ti_3C_2Br_2$, and $Ti_3C_2Cl_2$ at 50, 100, 200, 500 and 1000 mV s^{-1} scan rates, (f) cycling stability at a current density of 5 mA cm^{-2}. Reproduced from ref. 81 with permission from [Elsevier], copyright [2024].

surface functional groups can be effectively modulated through fluorine-free etching and supramolecular self-assembly, thereby enhancing their performance for practical applications.

MXene exhibits electrical conductivity comparable to graphene and carbon nanotubes, while demonstrating lower density compared to conventional metallic electromagnetic interference (EMI) shielding materials, as shown in Table 1. This unique combination of properties renders MXene an ideal candidate for lightweight applications, particularly in weight-sensitive aerospace engineering.[53,88] More importantly, the synergistic integration of controllable interlayer spacing and tunable surface functional groups enables unprecedented flexibility in engineering the absorption/reflection balance of electromagnetic waves through dipole polarization and interfacial charge transfer mechanisms.[50,89] Such tunability facilitates superior EMI shielding performance across multiple spectral frequency ranges (RF region, X-band, Ku-band, Ka-band, V-band, and W-band), outperforming most existing two-dimensional nanomaterials.[90]

Given the multiple factors affecting electromagnetic shielding performance, we investigated four commonly used EMI shielding materials, with a particular focus on thickness as

3 MXene in the field of EMI shielding applications

3.1 Comparison of MXene with other EMI shielding materials

The electromagnetic shielding performance of materials is primarily influenced by factors such as electrical conductivity and thickness. However, in recent years, the requirements for electromagnetic shielding materials have expanded beyond high SE to include lightweight properties, impedance matching to minimize reflection and excellent stability in operational environments. Although MXenes are prone to oxidation, their

Table 1 Comparison of MXene with other EMI shielding materials

Materials	Conductivity (S cm^{-1})	Density	Synthesis methods	Advantages	Limitations
MXene[53,82]	1500–20 000	Low	Fluoride etching, non-fluoride etching	High conductivity, lightweight, tunable interlayer spacing	Susceptible to oxidation, high cost, difficult to use for large-scale
Graphene[83,84]	10 000–20 000	Low	Bottom-up (CVD[a]), top-down (exfoliation methods)	High conductivity, large surface area	High cost, limited scalability, difficult to use for large-scale
Carbon nanotubes[85]	10^3–10^4	Low	CVD[a] arc discharge	High conductivity, high aspect ratio	High cost, difficult to disperse uniformly
Metal (*e.g.*, Cu[86,87])	5.96×10^5	High	Hydrometallurgy, pyrometallurgy, electrochemical deposition	High SE, low cost, high-thermal conductivity	High density, corrosion susceptibility

[a] Chemical vapor deposition.

a representative influencing factor in this study. Liu *et al.* developed MXene foam through hydrazine-induced foaming, demonstrating a significant enhancement in EMI shielding effectiveness from 53 dB for a 6-μm-thick MXene film to 70 dB for the foamed structure (60 μm).[46] Regarding graphene-based materials, due to the challenges in directly foaming graphene films, graphene oxide (GO) is typically employed as a precursor. Following this approach, Shen *et al.* fabricated graphene foam using a similar hydrazine-induced foaming process with GO films.[91] However, despite increasing the thickness from 20 μm to 300 μm, the resulting graphene foam only achieved an EMI SE of 25.2 dB. Reo Yanagi *et al.* prepared carbon nanotube-based composite aerogels *via* freeze-drying methodology, exhibiting a shielding effectiveness exceeding 30 dB at 40 wt% CNTs content, though requiring a substantial thickness of 3 mm.[92] While bulk metallic materials possess high electrical conductivity, low manufacturing costs, and excellent electromagnetic shielding performance, their practical application in EMI shielding is limited by inherent drawbacks such as high density and susceptibility to corrosion.[87,93] Collecitively, MXene emerges as a promising candidate for EMI shielding applications, demonstrating superior performance characteristics among the investigated materials.

3.2 MXene-based composite materials in the field of electromagnetic shielding applications

Due to its exceptional electrical conductivity, MXene and its composite materials have become prominent in the field of EMI shielding research in recent years. MXene-based EMI shielding materials exhibit excellent performance characteristics including wide frequency response, lightweight, high-temperature stability, and corrosion resistance. Consequently, these materials hold significant potential for diverse applications across various sectors such as electronic equipment, medical and military technologies, and aerospace.[46,94–99]

Electromagnetic waves can disrupt the normal operation of electronic equipment, potentially leading to equipment failure or data loss. This interference is particularly critical in wireless communication devices and sensitive electronics, where it can degrade performance and stabilize it.[100,101] Therefore, mitigating electromagnetic interference is crucial for enhancing the safety and reliability of electronic devices.

For most electronic products, electromagnetic shielding materials must achieve an effective shielding effectiveness (SE) of at least 20 dB to ensure functionality.[102] Flexible MXene-based composite films are promising candidates for stabilizing the operation of wearable electronic devices. Jiao *et al.* prepared aqueous polyurethane/natural rubber/MXene composite films using vacuum-assisted filtration, achieving an average EM shielding effectiveness of 76.1 dB.[103] Additionally, these films exhibited excellent mechanical properties and photo-thermal healing ability, suggesting potential applications in EM shielding devices and flexible wearable electronics. Qu *et al.* developed heterogeneous multifunctional composite films by integrating MXene with silver nanowires and nano-silver flakes, achieving an EM shielding effectiveness of 70.96 dB.[104] These materials also displayed superior thermal conductivity, flame retardance, high temperature resistance, and mechanical properties, indicating significant potential for use in highly integrated advanced flexible electronics. Liu *et al.* encapsulated MXene materials in shape-stable phase change materials, resulting in MXene-based EM shielding composite phase change materials with an EM shielding effectiveness of 64.7 dB and enhanced thermal management capabilities.[105] Du *et al.* constructed a composite phase change material with 48.1 dB EM shielding effectiveness and thermal management capabilities from a modified MXene-based nanocomposite elastomer.[106] This ultra-flexible generator, capable of real-time detection of human body motion and physical signals, was assembled using sensors from this composite. Sang *et al.* explored a flexible polyvinylidene fluoride (PVDF)/MXene/polyimide (PI) wearable electronic device with a 40 dB EM shielding effectiveness, suitable for body monitoring and thermal therapy.[107] Zhuang *et al.* successfully fabricated a film with high strength and a dense structure by limiting the wet film thickness to less than 60 μm to prevent the formation of a masking effect.[108] The film, with a thickness of 1 μm, demonstrated an EMI shielding performance of 48.4 dB in the X-band.

'Sandwich' structures have emerged as a highly effective design for EMI shielding due to their unique layered architecture, which combines multiple functional materials to achieve superior performance. Vacuum-assisted filtration (VAF) is instrumental in the creation of multilayer films, particularly 'sandwich' films, and in the uniform deposition of functional fillers. Leveraging hydrogen bonding and covalent cross-linking within MXene lamellae, Hu *et al.* employed vacuum-assisted filtration and impregnation to create MXene-aramid nanofiber composite films with a 'sandwich' structure,[109] as depicted in Fig. 6(a). This unique layered structure provides excellent mechanical properties and stability in Fig. 6(d), and the composite film achieves an electromagnetic shielding effectiveness of 46.1 dB and a tensile strength of up to 302.1 MPa when the film thickness is approximately 23.3 μm.

Li *et al.* successfully fabricated sandwich films using VAF, demonstrating exceptional flexibility and high electromagnetic shielding capabilities.[110] Their study delved into the impact of varying quantities of 'sandwich layer' (MXene) and 'core layer' (CNTs/SA) on the electromagnetic shielding efficacy of composite films. The electrical conductivity of the composite films exhibits a proportional increase with the MXene content, owing to the 1D CNTs' dual role in effectively mitigating the self-stacking of the 2D MXene nanosheets and establishing a seamless conductive network with the MXene, ultimately enhancing electron transport. Notably, composite films containing 15 mg of MXene and a total of 6 mg of CNTs/SA (with a mass ratio of CNTs to SA of 6 : 4) exhibited outstanding electromagnetic shielding performance at a thickness of 12 μm (with a shielding effectiveness of 61.3 dB and specific shielding effectiveness per unit thickness of 2.34×10^5 dB cm^2 g^{-1}).[110,111] VAF enables the development of multifunctional 'sandwich' films, necessitating the incorporation of appropriate functional fillers within the functional layers. In contrast to previously established electromagnetic shielding 'sandwich' films, Ding *et al.* introduced a multifunctional composite film that exhibits superior electromagnetic interference shielding capabilities (nearly 70 dB), as well as optical, electrical, and magnetic-thermal conversion and storage properties, as shown in Fig. 7.[112] They optimized the synergistic interaction between one-dimensional silver nanowires and two-dimensional MXene nanosheets. This optimization is attributed to the exceptional electrical conductivity of both materials, which enhances charge transport across their interfaces, thereby minimizing energy loss. Furthermore, the integration of MXene reduces the contact between silver nanowires, effectively lowering their contact resistance and consequently improving the overall electrical conductivity of the composite. Additionally, both materials possess excellent thermal conductivity, and their

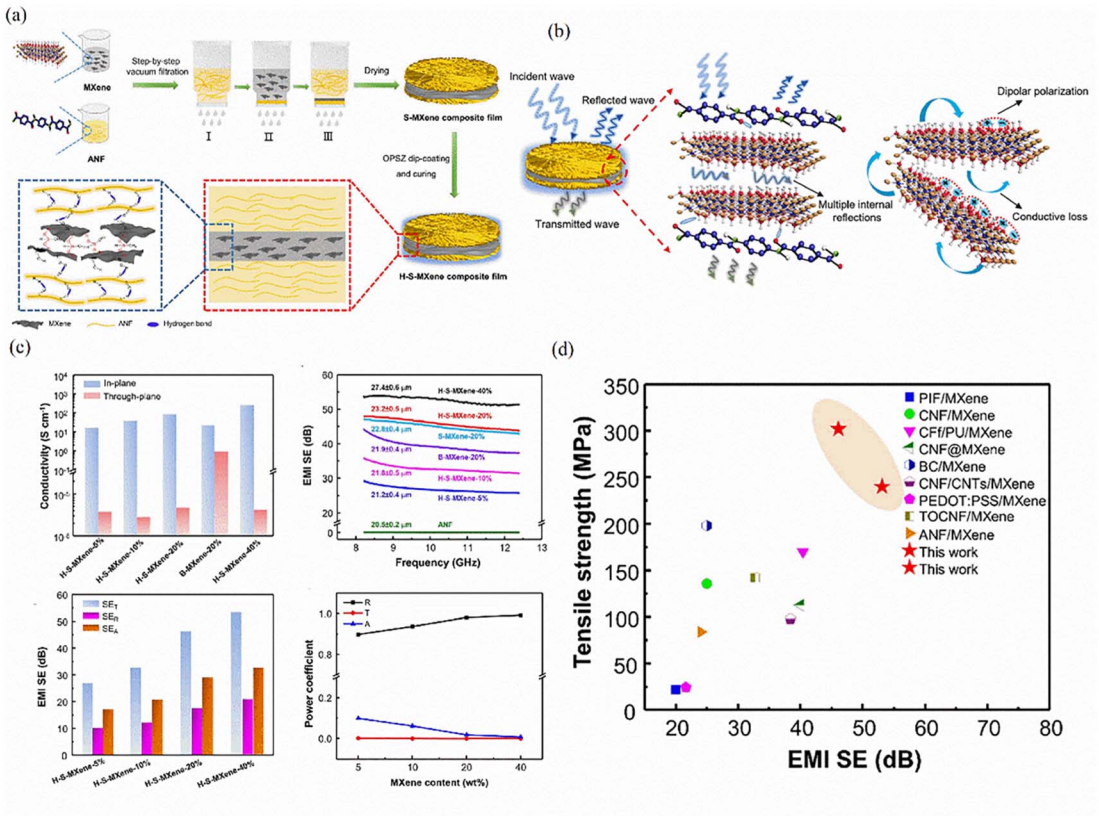

Fig. 6 (a) Schematic diagram of the preparation of this composite film, (b) diagram of electromagnetic interference shielding mechanism of this composite film, (c) characterization of the conductivity and electromagnetic shielding properties of this composite film, (d) mechanical properties and electromagnetic shielding properties of this composite film in comparison with other electromagnetic shielding materials under study. Adapted with permission from reference. Reproduced from ref. 109 with permission from [American Chemical Society], copyright [2022].

combination facilitates the formation of an efficient thermal conductive network.

Medical devices frequently generate electromagnetic radiation that can interfere with nearby electronic equipment or adversely affect patients. Utilizing MXene-based electromagnetic shielding materials can effectively mitigate this radiation, thereby reducing its impact on both devices and human health. Additionally, biomedical sensors, which often rely on highly

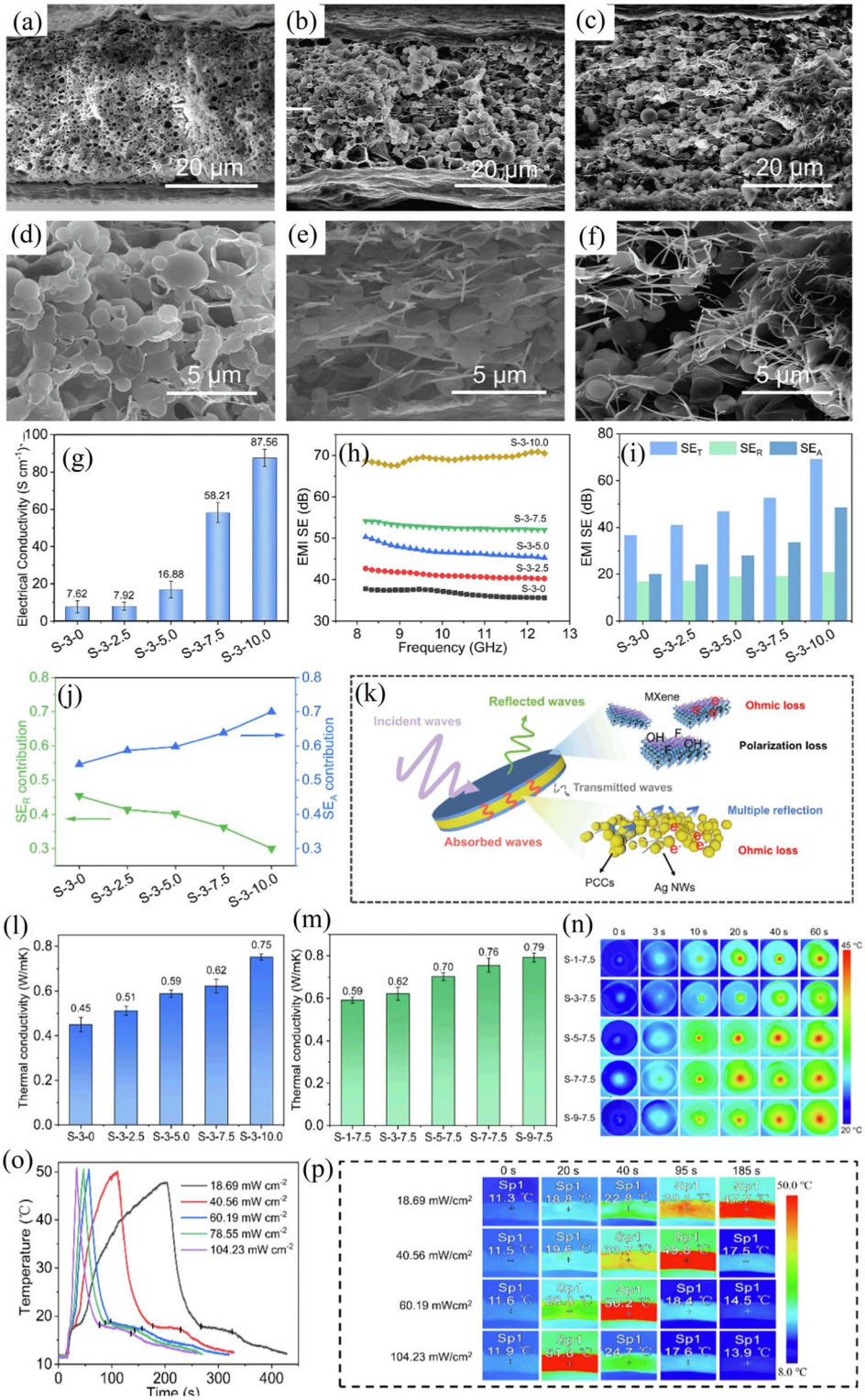

Fig. 7 (a–f) Scanning electron microscopy (SEM) schematic of sandwich composite films, (g–j) characterization of conductivity and electromagnetic shielding properties of sandwich composite films, (k) electromagnetic shielding mechanism diagram of sandwich composite films, (l–p) photothermal characterization of sandwich composite films. Reproduced from ref. 112 with permission from [Elsevier], copyright [2024].

sensitive electrical signals to detect biological indicators, can be compromised by surrounding electromagnetic interference. MXene-based shielding materials can effectively counteract this interference, enhancing the accuracy and reliability of the sensors. Capitalizing on the distinctive properties of MXene materials, alongside thermoelectric effects and self-heating technology, Zhang *et al.* developed a wearable thermoelectric respiratory sensor based on MXene.[113] This sensor dynamically monitors respiration by generating an electrical potential through the temperature difference between respiratory gas and ambient temperature, achieving an impressive electromagnetic shielding effectiveness of 59 dB. This innovative sensing technology holds significant potential for advancing medical monitoring and health management.[113–115]

MXene nanosheets are recognized for their excellent electrical conductivity and electromagnetic shielding properties, which enable them to absorb, reflect, and scatter electromagnetic waves effectively. These properties make them ideal for manufacturing lightweight, high-strength components for aerospace and military applications, such as aerogels that enhance the safety and multifunctionality of aerospace materials. This is due to the rich porous structure and high specific surface area of the aerogel which facilitates the enhancement of multiple reflections.[116]

In general, for lightweight electromagnetic shielding materials, it is insufficient to evaluate their capability solely based on the numerical values of electromagnetic shielding effectiveness (SE). It is also essential to consider the density (ρ) and thickness (t) of these porous materials. Consequently, metrics such as specific shielding effectiveness (SSE = SE/ρ) and absolute shielding effectiveness (SSEt = SSE/t) have been introduced to assess the performance of these materials.[28] Wu *et al.* developed

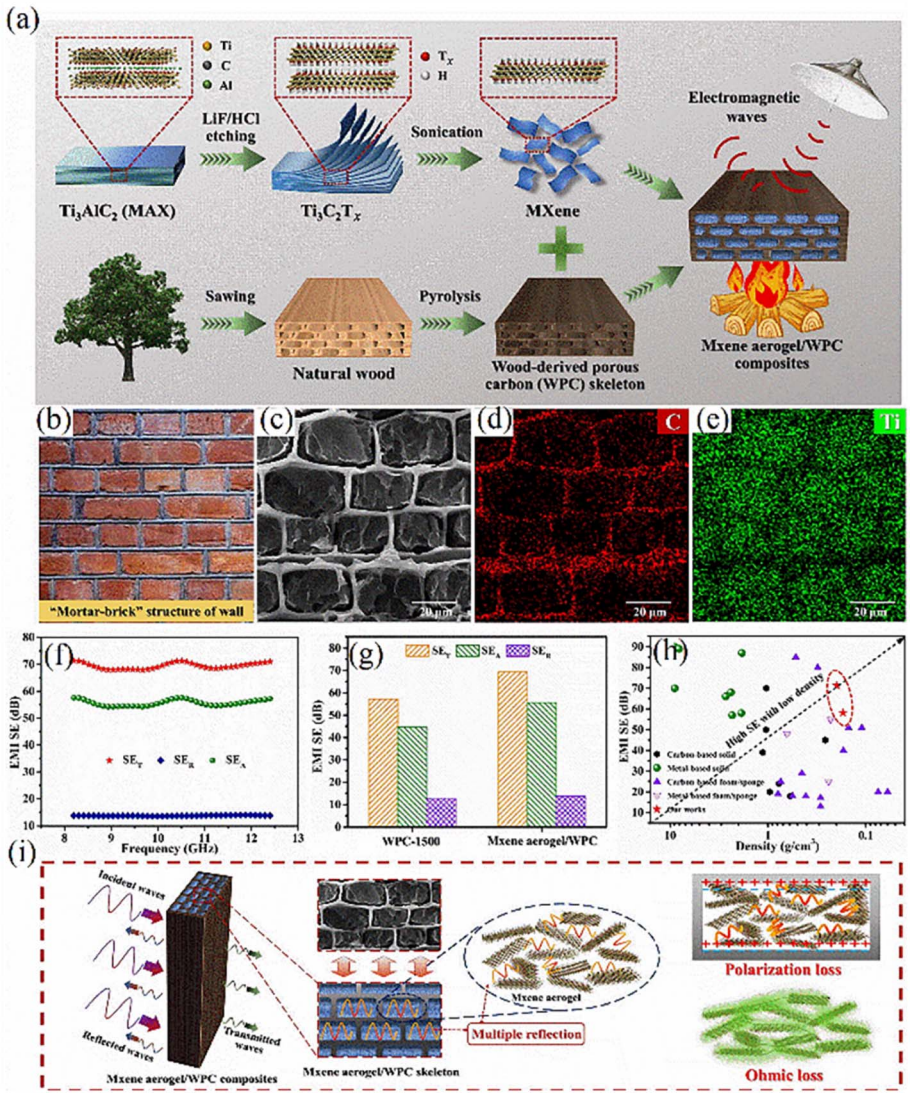

Fig. 8 (a) Schematic of the preparation of this biocarbon-based composite; (b–e) SEM images and elemental mapping of C and Ti of the composite; (f–h) EMI SE of the composite; (i) schematic of the electromagnetic shielding of the composite. Reproduced from ref. 118 with permission from [Elsevier], copyright [2024].

an aerogel with a hierarchical pore structure by integrating MXene and chitosan, achieving an electromagnetic shielding effectiveness of approximately 61.4 dB and a specific shielding effectiveness as high as 5155.46 dB cm^3 g^{-1} with only 3 mm thickness.[117] Shells exhibit excellent mechanical properties due to their unique 'sand-brick' structure, characterized by the alternating arrangement of inorganic calcium carbonate nanosheets ('bricks') and organic polymers ('slurry'). Inspired by this natural design, Liang *et al.* crafted an aerogel with a wall-like structure using a porous carbon skeleton as the 'mortar' and a 3D MXene aerogel as the 'brick',[118] as depicted in Fig. 8(a–e). This low-density 'mortar-brick' structure not only provides the aerogel with an electromagnetic interference shielding efficiency of up to 71.3 dB but also demonstrates exceptional mechanical and thermal insulation properties. Such multifunctional biocarbon-based composite materials hold significant promise for advanced applications in aerospace and defense industries.

Despite the numerous advantages of MXene, its inferior oxidation stability inevitably leads to a gradual decline in electrical conductivity, thereby compromising long-term EMI shielding performance. Recently, supramolecular self-assembly techniques have been explored to integrate MXene with complementary materials through non-covalent interactions such as hydrogen bonding and electrostatic forces. This strategic approach not only enhances their synergistic performance in practical applications but also effectively prolongs the material's service life by mitigating oxidative degradation pathways.[119,120] Zhu *et al.* utilized metal ions (K^+) to induce the self-assembly of MXene nanosheets and vacuum impregnated the MXene-K^+ aerogels obtained through freeze-drying technology into molten paraffin to prepare composite phase change materials with electromagnetic shielding properties.[121] Thanks to the effective binding between K^+ and the hydroxyl groups on the MXene nanosheets, the MXene nanosheets were able to arrange in an orderly manner. When the weight ratio of KCl to MXene reached 4 : 1, the material exhibited excellent electromagnetic shielding performance, achieving a shielding effectiveness of 57.7 dB. Tang *et al.* successfully fabricated a porous thin film with exceptional antioxidative properties through electrostatic self-assembly of MXene and GO followed by thermal annealing in an inert atmosphere.[122] The resulting composite material demonstrates remarkable electromagnetic shielding performance (47 dB) at an ultra-thin thickness of 15 μm. Notably, the combined process of electrostatic self-assembly and thermal annealing effectively removes hydroxyl groups from both MXene and GO nanosheets, thereby endowing the porous structure with long-term antioxidative stability (12 months duration).

MXene-based electromagnetic shielding composites play a pivotal role in electronic science and technology, and their research and development progress and practical application prospects demonstrate an exceptionally broad trajectory. With the continuous advancement of science and technology, as well as the expanding societal demand, this field is poised to experience more in-depth academic research and a wider range of practical applications.

4 Conclusions

In conclusion, this paper reviews the structure, properties, preparation methods, and research progress of MXene-based electromagnetic shielding materials. MXene, as a two-dimensional material with a unique structure and properties, holds significant potential for future developments in the fields of electromagnetic shielding and wave-absorbing materials. Notably, the highly adjustable layer spacing of two-dimensional MXene provides a unique opportunity for its application in electromagnetic shielding and wave absorption. By manipulating the layer spacing of 2D MXene, the absorption or reflection of electromagnetic radiation within specific frequency ranges can be optimized. This capability enables MXene to effectively shield electromagnetic waves, thus offering protection for electronic equipment and communication systems. Furthermore, the excellent electrical conductivity of MXene allows its use as a conductive layer in electromagnetic shielding materials, facilitating the effective guidance and dispersion of electromagnetic radiation. Most importantly, the lightweight structure of two-dimensional MXene enables efficient electromagnetic shielding performance without significantly increasing weight, laying the groundwork for its future integration into lightweight electronic devices.

The preparation process of MXene is relatively complex, involving high costs and extended preparation times, which hinder its scalability for industrial applications. Additionally, MXene is vulnerable to morphological and property alterations due to environmental factors such as humidity and temperature. Most critically, prolonged exposure to the environment can lead to a gradual degradation in electrical conductivity due to its oxidation sensitivity, adversely affecting its electromagnetic shielding capabilities. Consequently, it is essential to explore modifications in the preparation of MXene to enhance its oxidation resistance by altering its surface groups. Currently, the fluorine-containing etching method is a prevalent and efficient technique for preparing MXene; however, the environmental impact of the acidic and fluorine-containing compounds used in this process cannot be overlooked. Thus, the development of fluorine-free etching techniques and green preparation methods represents a viable approach for producing environmentally friendly MXene with enhanced performance.

While the high conductivity of MXene contributes to its exceptional electromagnetic shielding performance in composites, it can also cause electromagnetic waves to be reflected due to impedance mismatch induced by the material's highly conductive surface when exposed to air, leading to secondary pollution of electromagnetic waves. Consequently, recent research has increasingly focused on MXene-based electromagnetic shielding composites that exhibit 'low reflection and high absorption' characteristics. Specifically, to address the 'low reflection characteristics', magnetic particles are often introduced to mitigate the strong electromagnetic reflection caused by MXene's high conductivity and to improve the conditions of impedance matching, though this approach

can compromise overall shielding performance. Future studies could investigate how the electrical conductivity of MXene is influenced by the type and shape of magnetic particles. Further exploration could also focus on the synergistic effects of magnetic particles with MXene, particularly in relation to their combined impact on electromagnetic shielding applications in carbon-based materials.

Data availability

No primary research results, software or code have been included and no new data were generated or analyzed as part of this review.

Author contributions

Yao Gan: writing – original draft, review & editing. Yuzhu Xiong: editing, supervision and funding acquisition.

Conflicts of interest

There are no conflicts to declare.

Acknowledgements

This work is supported by the National Natural Science Foundation of China (52063006).

References

1 M. K. Han and Y. Gogotsi, *Carbon*, 2023, **204**, 17–25.
2 X. Y. Wu, T. X. Tu, Y. Dai, P. P. Tang, Y. Zhang, Z. M. Deng, L. L. Li, H. B. Zhang and Z. Z. Yu, *Nano–Micro Lett.*, 2021, **13**, 15.
3 R. K. Amineh, *Electronics*, 2020, **9**, 4.
4 S. H. Ryu, B. Park, Y. K. Han, S. J. Kwon, T. Kim, R. Lamouri, K. H. Kim and S. B. Lee, *J. Mater. Chem. A*, 2022, **10**, 4446–4455.
5 W. Gao, N. Zhao, T. Yu, J. Xi, A. Mao, M. Yuan, H. Bai and C. Gao, *Carbon*, 2020, **157**, 570–577.
6 S. T. Gao, Y. C. Zhang, H. L. Xing and H. X. Li, *Chem. Eng. J.*, 2020, **387**, 124149.
7 B. Jiang, C. Qi, H. Yang, X. Wu, W. Yang, C. Zhang, S. Li, L. Wang and Y. Li, *Carbon*, 2023, **208**, 390–409.
8 Y. P. Sun, X. G. Liu, C. Feng, J. C. Fan, Y. H. Lv, Y. R. Wang and C. T. Li, *J. Alloys Compd.*, 2014, **586**, 688–692.
9 J. C. Lin, *IEEE Microwave Mag.*, 2016, **17**, 32–36.
10 P. Song, C. Liang, L. Wang, H. Qiu, H. Gu, J. Kong and J. Gu, *Compos. Sci. Technol.*, 2019, **181**, 107698.
11 J. Tao, J. Zhou, Z. Yao, Z. Jiao, B. Wei, R. Tan and Z. Li, *Carbon*, 2021, **172**, 542–555.
12 S. Wei, C. Zhou and L. Huang, *Laser Med. Sci.*, 2022, **38**, 25.
13 Y. Du, Y. Liu, A. Wang and J. Kong, *iScience*, 2023, **26**, 107873.
14 E. Calabrò, *Sustainability*, 2018, **10**, 3326.
15 M. Y. Peng and F. X. Qin, *J. Appl. Phys.*, 2021, **130**, 9.
16 G. R. Hu, Z. Q. Cen, Y. Z. Xiong and K. Liang, *Nanoscale*, 2023, **15**, 5579–5597.
17 D. D. L. Chung, *Mater. Chem. Phys.*, 2020, **255**, 11.
18 X. X. Wang, J. C. Shu, W. Q. Cao, M. Zhang, J. Yuan and M. S. Cao, *Chem. Eng. J.*, 2019, **369**, 1068–1077.
19 C. B. Liang, P. Song, A. J. Ma, X. T. Shi, H. B. Gu, L. Wang, H. Qiu, J. Kong and J. W. Gu, *Compos. Sci. Technol.*, 2019, **181**, 7.
20 M. Khazaei, A. Ranjbar, M. Arai, T. Sasaki and S. Yunoki, *J. Mater. Chem. C*, 2017, **5**, 2488–2503.
21 M. Naguib, M. Kurtoglu, V. Presser, J. Lu, J. J. Niu, M. Heon, L. Hultman, Y. Gogotsi and M. W. Barsoum, *Adv. Mater.*, 2011, **23**, 4248–4253.
22 M. Pumera and Z. Sofer, *Chem. Soc. Rev.*, 2017, **46**, 4450–4463.
23 M. F. Bhopal, D. W. Lee, A. U. Rehman and S. H. Lee, *J. Mater. Chem. C*, 2017, **5**, 10701–10714.
24 J. Halim, M. R. Lukatskaya, K. M. Cook, J. Lu, C. R. Smith, L. Näslund, S. J. May, L. Hultman, Y. Gogotsi, P. Eklund and M. W. Barsoum, *Chem. Mat.*, 2014, **26**, 2374–2381.
25 T. Wu, P. R. C. Kent, Y. Gogotsi and D. E. Jiang, *Chem. Mat.*, 2022, **34**, 4975–4982.
26 R. Khan and S. Andreescu, *Biosens. Bioelectron.*, 2024, **248**, 8.
27 Y. Gogotsi, *Chem. Mat.*, 2023, **35**, 8767–8770.
28 F. Shahzad, M. Alhabeb, C. B. Hatter, B. Anasori, S. M. Hong, C. M. Koo and Y. Gogotsi, *Science*, 2016, **353**, 1137–1140.
29 A. Lipatov, H. D. Lu, M. Alhabeb, B. Anasori, A. Gruverman, Y. Gogotsi and A. Sinitskii, *Sci. Adv.*, 2018, **4**, 7.
30 S. Jin, Y. T. Guo, F. L. Wang and A. G. Zhou, *MRS Bull.*, 2023, **48**, 245–252.
31 B. Anasori and M. Naguib, *MRS Bull.*, 2023, **48**, 238–244.
32 M. Naguib, V. N. Mochalin, M. W. Barsoum and Y. Gogotsi, *Adv. Mater.*, 2014, **26**, 992–1005.
33 J. G. Sun, B. B. Liu, Q. Zhao, C. H. Kirk and J. Wang, *Adv. Mater.*, 2023, **35**, 2306072.
34 S. J. Wu, H. Liu, Q. H. Wang, X. Y. Yin and L. X. Hou, *J. Alloys Compd.*, 2023, **945**, 11.
35 W. W. Liu, H. Li, Q. P. Zeng, H. N. Duan, Y. P. Guo, X. F. Liu, C. Y. Sun and H. Z. Liu, *J. Mater. Chem. A*, 2015, **3**, 3739–3747.
36 H. Shin, W. Eom, K. H. Lee, W. Jeong, D. J. Kang and T. H. Han, *ACS Nano*, 2021, **15**, 3320–3329.
37 Z. Y. Tan, W. Wang, M. K. Zhu, Y. C. Liu, Y. X. Yang, X. H. Ji and Z. K. He, *Desalination*, 2023, **548**, 116267.
38 F. T. Ran, T. L. Wang, S. Y. Chen, Y. Y. Liu and L. Shao, *Appl. Surf. Sci.*, 2020, **511**, 145627.
39 D. D. Zhao, Z. R. Chen, N. Fu and Z. L. Yang, *Mater. Today Sustain.*, 2023, **24**, 100523.
40 Q. Y. Yang, Z. Xu, B. Fang, T. Q. Huang, S. Y. Cai, H. Chen, Y. J. Liu, K. Gopalsamy, W. W. Gao and C. Gao, *J. Mater. Chem. A*, 2017, **5**, 22113–22119.
41 A. Iqbal, P. Sambyal and C. M. Koo, *Adv. Funct. Mater.*, 2020, **30**, 2000883.
42 N. Kubitza, C. Büchner, J. Sinclair, R. M. Snyder and C. S. Birkel, *ChemPlusChem*, 2023, **88**, e202300214.

43 Y. Gogotsi and B. Anasori, *ACS Nano*, 2019, **13**, 8491–8494.
44 X. J. Zeng, C. Zhao, X. Jiang, R. H. Yu and R. C. Che, *Small*, 2023, **19**, 10.
45 Q. Q. Wang, W. Q. Cao and M. S. Cao, *2D Mater.*, 2024, **11**, 012001.
46 J. Liu, H. B. Zhang, R. H. Sun, Y. F. Liu, Z. S. Liu, A. G. Zhou and Z. Z. Yu, *Adv. Mater.*, 2017, **29**, 6.
47 T. X. Zhou, C. Q. Zhao, Y. H. Liu, J. Huang, H. S. Zhou, Z. D. Nie, M. Fan, T. Y. Zhao, Q. F. Cheng and M. J. Liu, *ACS Nano*, 2022, **16**, 12013–12023.
48 J. Liu, Z. S. Liu, H. B. Zhang, W. Chen, Z. F. Zhao, Q. W. Wang and Z. Z. Yu, *Adv. Electron. Mater.*, 2020, **6**, 1901094.
49 K. Maleski, C. E. Ren, M. Q. Zhao, B. Anasori and Y. Gogotsi, *ACS Appl. Mater. Interfaces*, 2018, **10**, 24491–24498.
50 M. Ghidiu, M. R. Lukatskaya, M. Q. Zhao, Y. Gogotsi and M. W. Barsoum, *Nature*, 2014, **516**, 78–U171.
51 R. Khanal and S. Irle, *J. Chem. Phys.*, 2023, **158**, 10.
52 W. Eom, H. Shin, W. Jeong, R. B. Ambade, H. Lee and T. H. Han, *Mater. Horiz.*, 2023, **10**, 4892–4902.
53 T. S. Mathis, K. Maleski, A. Goad, A. Sarycheva, M. Anayee, A. C. Foucher, K. Hantanasirisakul, C. E. Shuck, E. A. Stach and Y. Gogotsi, *ACS Nano*, 2021, **15**, 6420–6429.
54 K. Y. Zhang, M. Y. Di, L. Fu, Y. Deng, Y. W. Du and N. J. Tang, *Carbon*, 2020, **157**, 90–96.
55 Z. Liu, M. L. Zhao, H. Lin, C. Dai, C. Y. Ren, S. J. Zhang, W. J. Peng and Y. Chen, *J. Mater. Chem. B*, 2018, **6**, 3541–3548.
56 W. J. Zhang, Y. H. Li, Y. X. Wang, Y. L. Wang, M. Kou, X. Y. Yang, Q. Q. Chu and K. Zhao, *Mater. Chem. Phys.*, 2023, **309**, 16.
57 X. Q. Qin, Z. G. Wu, J. W. Fang, S. S. Li, S. W. Tang and X. Y. Wang, *Appl. Surf. Sci.*, 2023, **616**, 11.
58 L. Li, Y. Lu, Z. T. Qian, Z. Y. Yang, S. F. Zong, Z. Y. Wang and Y. P. Cui, *Nanoscale*, 2021, **13**, 18546–18557.
59 Y. J. Dong, S. S. Li, X. Y. Li and X. Y. Wang, *Int. J. Biol. Macromol.*, 2021, **190**, 693–699.
60 O. S. Lee, M. E. Madjet and K. A. Mahmoud, *Nano Lett.*, 2021, **21**, 8510–8517.
61 X. Z. Wei, G. C. Song, M. H. Li, L. H. Li, Y. X. Lu, L. Zhang, D. Dai, T. Cai, K. Nishimura, C. T. Lin, N. Jiang and J. H. Yu, *Compos. Commun.*, 2023, **43**, 101729.
62 A. V. Mohammadi, J. Rosen and Y. Gogotsi, *Science*, 2021, **372**, 1165.
63 B. Anasori and Y. Gogotsi, *Graphene 2D Mater. Technol.*, 2022, **7**, 75–79.
64 M. Kurtoglu, M. Naguib, Y. Gogotsi and M. W. Barsoum, *MRS Commun.*, 2012, **2**, 133–137.
65 X. Y. Huang, W. N. Mu and C. Chang, *Environ. Sci. Pollut. Res.*, 2023, **30**, 52157–52168.
66 B. Soundiraraju and B. K. George, *ACS Nano*, 2017, **11**, 8892–8900.
67 X. Y. Zhang, W. Zhang and H. T. Zhao, *Int. J. Energy Res.*, 2022, **46**, 15559–15570.
68 Y. B. Wang, B. Zhou, Q. Tang, Y. Yang, B. Pu, J. Bai, J. Xu, Q. G. Feng, Y. Liu and W. Q. Yang, *Adv. Mater.*, 2024, **36**, 10.
69 K. Arole, J. W. Blivin, A. M. Bruce, S. Athavale, I. J. Echols, H. X. Cao, Z. Y. Tan, M. Radovic, J. L. Lutkenhaus and M. J. Green, *Chem. Commun.*, 2022, **58**, 10202–10205.
70 Y. Yao, Z. F. Wang, W. X. Wang, Y. T. Han and Z. G. Zhu, *Chem. Eng. J.*, 2024, **489**, 11.
71 Y. B. Li, H. Shao, Z. F. Lin, J. Lu, L. Y. Liu, B. Duployer, P. Persson, P. Eklund, L. Hultman, M. Li, K. Chen, X. H. Zha, S. Y. Du, P. Rozier, Z. F. Chai, E. Raymundo-Piñero, P. L. Taberna, P. Simon and Q. Huang, *Nat. Mater.*, 2020, **19**, 894.
72 S. Ali, S. K. Thakur, A. Sarkar and S. Shekhar, *Environ. Chem. Lett.*, 2016, **14**, 291–315.
73 N. Xue, X. S. Li, L. Y. Han, H. Zhu, X. Y. Zhao, J. Zhuang, Z. L. Gao and X. T. Tao, *J. Mater. Chem. A*, 2022, **10**, 7960–7967.
74 S. J. Kim, H. J. Koh, C. E. Ren, O. Kwon, K. Maleski, S. Y. Cho, B. Anasori, C. K. Kim, Y. K. Choi, J. Kim, Y. Gogotsi and H. T. Jung, *ACS Nano*, 2018, **12**, 986–993.
75 T. F. Li, L. L. Yao, Q. L. Liu, J. J. Gu, R. C. Luo, J. H. Li, X. D. Yan, W. Q. Wang, P. Liu, B. Chen, W. Zhang, W. Abbas, R. Naz and D. Zhang, *Angew. Chem., Int. Ed.*, 2018, **57**, 6115–6119.
76 A. D. Wu, T. H. Wang, L. Zhang, C. Chen, Q. M. Li, X. H. Qu and Y. C. Liu, *Int. J. Miner. Metall. Mater.*, 2024, **31**, 1752–1765.
77 J. Z. Jiang, S. S. Bai, J. Zou, S. Liu, J. P. Hsu, N. Li, G. Y. Zhu, Z. C. Zhuang, Q. Kang and Y. Z. Zhang, *Nano Res.*, 2022, **15**, 6551–6567.
78 M. H. Sheng, X. Q. Bin, Y. W. Yang, Z. Chen and W. X. Que, *Adv. Mater. Technol.*, 2024, **9**, 2301694.
79 S. Yang, P. P. Zhang, F. X. Wang, A. G. Ricciardulli, M. R. Lohe, P. W. M. Blom and X. L. Feng, *Angew. Chem., Int. Ed.*, 2018, **57**, 15491–15495.
80 M. Li, J. Lu, K. Luo, Y. B. Li, K. K. Chang, K. Chen, J. Zhou, J. Rosen, L. Hultman, P. Eklund, P. Persson, S. Y. Du, Z. F. Chai, Z. R. Huang and Q. Huang, *J. Am. Chem. Soc.*, 2019, **141**, 4730–4737.
81 J. M. Zhu, S. L. Zhu, Z. D. Cui, Z. Y. Li, S. L. Wu, W. Xu, T. Ba, Y. Q. Liang and H. Jiang, *Energy Storage Mater.*, 2024, **70**, 10.
82 B. Anasori and Y. Gogotsi, *Graphene 2D Mater.*, 2022, **7**, 75–79.
83 Y. Yu, X. Liu, D. Lu, T. Liu, Y. Li and Z. Wu, *Carbon*, 2025, **236**, 120093.
84 A. Ibrahim, A. Klopocinska, K. Horvat and Z. A. Hamid, *Polymers*, 2021, **13**, 32.
85 M. Syduzzaman, M. S. Islam Saad, M. F. Piam, T. A. Talukdar, T. T. Shobdo and N. M. Pritha, *Results Mater.*, 2025, **25**, 100654.
86 R. Dang, L. L. Song, W. J. Dong, C. R. Li, X. B. Zhang, G. Wang and X. B. Chen, *ACS Appl. Mater. Interfaces*, 2014, **6**, 622–629.
87 S. H. Lee, S. Yu, F. Shahzad, J. P. Hong, W. N. Kim, C. Park, S. M. Hong and C. M. Koo, *Compos. Sci. Technol.*, 2017, **144**, 57–62.
88 B. Anasori, M. R. Lukatskaya and Y. Gogotsi, *Nat. Rev. Mater.*, 2017, **2**, 17.

89 A. Iqbal, F. Shahzad, K. Hantanasirisakul, M. K. Kim, J. Kwon, J. Hong, H. Kim, D. Kim, Y. Gogotsi and C. M. Koo, *Science*, 2020, **369**, 446.
90 A. Iqbal, J. Kwon, T. Hassan, S. W. Park, W. H. Lee, J. M. Oh, J. Hong, J. Lee, S. M. Naqvi, U. Zafar, S. J. Kim, J. H. Park, M. K. Kim and C. M. Koo, *Adv. Funct. Mater.*, 2024, 2409346, DOI: 10.1002/adfm.202409346.
91 B. Shen, Y. Li, D. Yi, W. T. Zhai, X. C. Wei and W. G. Zheng, *Carbon*, 2016, **102**, 154–160.
92 R. Yanagi, T. Segi, A. Ito, T. Ueno and K. Hidaka, *Jpn. J. Appl. Phys.*, 2021, **60**, 8.
93 H. R. Zhao, J. H. Ding, M. Zhou and H. B. Yu, *ACS Appl. Nano Mater.*, 2021, **4**, 3075–3086.
94 K. Huang, Z. J. Li, J. Lin, G. Han and P. Huang, *Chem. Soc. Rev.*, 2018, **47**, 5109–5124.
95 X. L. Li, X. W. Yin, S. Liang, M. H. Li, L. F. Cheng and L. T. Zhang, *Carbon*, 2019, **146**, 210–217.
96 Y. Li, K. Y. Wu, M. Zhang, X. L. Yang, W. Feng, P. Wang, K. Li, Y. Q. Zhan and Z. W. Zhou, *Ceram. Int.*, 2022, **48**, 37032–37038.
97 W. J. Ma, W. R. Cai, W. H. Chen, P. J. Liu, J. F. Wang and Z. X. Liu, *Chem. Eng. J.*, 2021, **426**, 9.
98 A. Iqbal, J. Kwon, M. K. Kim and C. M. Koo, *Mater. Today Adv.*, 2021, **9**, 15.
99 Z. J. Xu, X. Ding, S. K. Li, F. Z. Huang, B. J. Wang, S. P. Wang, X. Zhang, F. H. Liu and H. Zhang, *ACS Appl. Mater. Interfaces*, 2022, **14**, 40396–40407.
100 F. Shahzad, A. Iqbal, H. Kim and C. M. Koo, *Adv. Mater.*, 2020, **32**, 2002159.
101 Y. H. Zhang, Y. Zhang, H. M. Liu, D. Li, Y. B. Wang, C. C. Xu, Y. P. Tian and H. J. Meng, *Int. J. Miner. Metall. Mater.*, 2024, **31**, 2508–2517.
102 D. D. L. Chung, *Mater. Chem. Phys.*, 2020, **255**, 123587.
103 C. Y. Jiao, Z. M. Deng, P. Min, J. J. Lai, Q. Q. Gou, R. Gao, Z. Z. Yu and H. B. Zhang, *Carbon*, 2022, **198**, 179–187.
104 Y. F. Qu, X. Li, X. Wang and H. Q. Dai, *Compos. Sci. Technol.*, 2022, **230**, 10.
105 H. B. Liu, R. L. Fu, X. Q. Su, B. Y. Wu, H. Wang, Y. Xu and X. H. Liu, *Compos. Sci. Technol.*, 2021, **210**, 108835.
106 Y. Z. Du, X. D. Wang, X. Y. Dai, W. X. Lu, Y. S. Tang and J. Kong, *J. Mater. Sci. Technol.*, 2022, **100**, 1–11.
107 M. Sang, S. Liu, W. W. Li, S. Wang, J. Li, J. Li, S. H. Xuan and X. L. Gong, *Composites, Part A*, 2022, **153**, 11.
108 Z. T. Zhuang, H. W. Chen and C. Li, *ACS Nano*, 2023, **17**, 10628–10636.
109 J. A. Hu, C. Y. Liang, J. D. Li, C. W. Lin, Y. J. Liang and D. W. Dong, *ACS Appl. Mater. Interfaces*, 2022, **14**, 33817–33828.
110 X. Y. Li, Z. F. Ma, L. L. Wang, S. K. Li, Y. H. Duan and M. H. Wu, *J. Mater. Sci.*, 2024, **59**, 1968–1988.
111 H. Chen, L. Y. Yu, Z. F. Lin, Q. Z. Zhu, P. Zhang, N. Qiao and B. Xu, *J. Mater. Sci.*, 2020, **55**, 1148–1156.
112 Y. Ding, X. Lu, S. Liu, H. Wu, X. X. Sheng, X. L. Li and J. P. Qu, *Composites, Part A*, 2022, **163**, 12.
113 C. R. Zhang, P. A. Zong, Z. S. Ge, Y. M. Ge, J. Zhang, Y. J. Rao, Z. G. Liu and W. Huang, *Nano Energy*, 2023, **118**, 12.
114 C. C. Jiang, J. Y. Chen, X. J. Lai, H. Q. Li, X. R. Zeng, Y. N. Zhao, Q. T. Zeng, J. F. Gao, Z. Z. Wu and Y. K. Qiu, *Chem. Eng. J.*, 2022, **434**, 9.
115 T. S. Peng, S. C. Wang, Z. G. Xu, T. T. Tang and Y. Zhao, *ACS Omega*, 2022, **7**, 29161–29170.
116 L. Y. Zhang, H. Y. Jin, H. X. Liao, R. Zhang, B. C. Wang, J. Y. Xiang, C. P. Mu, K. Zhai, T. Y. Xue and F. S. Wen, *Int. J. Miner. Metall. Mater.*, 2024, **31**, 1912–1921.
117 S. Q. Wu, D. M. Chen, W. B. Han, Y. S. Xie, G. D. Zhao, S. Dong, M. Y. Tan, H. Huang, S. B. Xu, G. Q. Chen, Y. Cheng and X. H. Zhang, *Chem. Eng. J.*, 2022, **446**, 137093.
118 C. B. Liang, H. Qiu, P. Song, X. T. Shi, J. Kong and J. W. Gu, *Sci. Bull.*, 2020, **65**, 616–622.
119 F. Gholamirad, J. Q. Ge, M. Sadati, G. A. Wang and N. Taheri-Qazvini, *ACS Appl. Mater. Interfaces*, 2022, 49158–44917, DOI: 10.1021/acsami.2c14019.
120 J. R. Zhao, Z. Wang, H. Wang, Y. Li and C. Q. Fang, *Colloids Surf., A*, 2023, **659**, 130841.
121 C. B. Zhu, Y. R. Hao, H. Wu, M. N. Chen, B. Q. Quan, S. Liu, X. P. Hu, S. L. Liu, Q. H. Ji, X. Lu and J. P. Qu, *Nano–Micro Lett.*, 2025, **17**, 16.
122 X. W. Tang, J. T. Luo, Z. W. Hu, S. J. Lu, X. Y. Liu, S. S. Li, X. Zhao, Z. H. Zhang, Q. Q. Lan, P. M. Ma, Z. C. Wang and T. X. Liu, *Nano Res.*, 2023, **16**, 1755–1763.